Nanoscale Res Lett (2010) 5:773–780
DOI 10.1007/s11671-010-9556-7

NANO EXPRESS

Effect of Size-Dependent Thermal Instability on Synthesis of Zn_2SiO_4-SiO_x Core–Shell Nanotube Arrays and Their Cathodoluminescence Properties

Chun Li · Yoshio Bando · Benjamin Dierre · Takashi Sekiguchi · Yang Huang · Jing Lin · Dmitri Golberg

Received: 21 December 2009 / Accepted: 28 January 2010 / Published online: 10 February 2010

Abstract Vertically aligned Zn_2SiO_4-SiO_x ($x < 2$) core–shell nanotube arrays consisting of Zn_2SiO_4-nanoparticle chains encapsulated into SiO_x nanotubes and SiO_x-coated Zn_2SiO_4 coaxial nanotubes were synthesized via one-step thermal annealing process using ZnO nanowire (ZNW) arrays as templates. The appearance of different nanotube morphologies was due to size-dependent thermal instability and specific melting of ZNWs. With an increase in ZNW diameter, the formation mechanism changed from decomposition of "etching" to Rayleigh instability and then to Kirkendall effect, consequently resulting in polycrystalline Zn_2SiO_4-SiO_x coaxial nanotubes, single-crystalline Zn_2SiO_4-nanoparticle-chain-embedded SiO_x nanotubes, and single-crystalline Zn_2SiO_4-SiO_x coaxial nanotubes. The difference in spatially resolved optical properties related to a particular morphology was efficiently documented by means of cathodoluminescence (CL) spectroscopy using a middle-ultraviolet emission at 310 nm from the Zn_2SiO_4 phase.

Keywords Nano-template · Core–shell nanotube · Cathodoluminescence · Zinc Silicate · Rayleigh instability · Kirkendall effect

Electronic supplementary material The online version of this article (doi:10.1007/s11671-010-9556-7) contains supplementary material, which is available to authorized users.

C. Li (✉) · Y. Bando · Y. Huang · J. Lin · D. Golberg
World Premier International Center for Materials Nanoarchitectonics (MANA), National Institute for Materials Science, Namiki 1-1, Tsukuba, Ibaraki 305-004, Japan
e-mail: LI.Chun@nims.go.jp; whulic@gmail.com

B. Dierre · T. Sekiguchi
Advanced Electronic Materials Center, National Institute for Materials Science (NIMS), Namiki 1-1, Tsukuba, Ibaraki 305-0044, Japan

Introduction

Nanotubes made of carbon and diverse inorganic compounds have continuously attracted significant attention due to their unique fundamental physical properties and many potential applications [1–3]. Inorganic nanotube generation strategy can generally be classified into two categories: first, one-step self-organization such as self-rolling and/or Ostwald ripening; second, two-step template-based fabrication through either scarification or recently developed solid-state reaction utilizing the Kirkendall effect [4–6]. From a viewpoint of final device integration, aligned nanotube arrays are highly desirable. In addition to the direct epitaxial growth of nanotube arrays on lattice-matched substrates, a solid-state reaction under thermal annealing and using readily available nanostructure arrays as templates could be an efficient way to generate novel chemically complex, multiphase nanotube arrays. However, due to a considerable increase in the surface-to-volume ratio with decreasing a nanomaterial size, size-dependent thermal stability and melting of the nanostructured templates during annealing must be carefully addressed.

ZnO nanowire (ZNW) arrays are one of the most common aligned nanostructures owing to their naturally preferable epitaxial growth at a relatively low temperature. They have widely been utilized as templates for the synthesis of lattice-matched GaN and SiC nanotubes, [7, 8] ZnO-related semiconducting heterojunctions [9, 10], and ZnO-based ternary compound nanostructures [11]. In most cases the latter have been considered to be even more important than pure-phase ZnO ones [4–6]. Although solid-state reactions by thermal annealing based on a ZNW template have been used to synthesize ZnO-based ternary compound nanotubes, [4–6, 11] no research has been

carried out on the influence of size-dependent template thermal stability on the final characteristics of such tubes.

In this study, this phenomenon was thoroughly demonstrated for the case of Zn_2SiO_4. While employing a one-step solid-state reaction and the ZNW array templates, vertically aligned Zn_2SiO_4-SiO_x core–shell nanotube arrays (ZSO), i.e., Zn_2SiO_4-nanoparticle chains encapsulated in SiO_x nanotubes, SiO_x-coated polycrystalline and single-crystalline Zn_2SiO_4 coaxial nanotubes were simultaneously obtained. Furthermore, a cathodoluminescence (CL) study, as a noninvasive and high spatial-resolution characterization tool, was employed to detect and analyze local structural and optical properties of the nanostructures. The structural and optical differences were effectively identified by transmission electron microscopy (TEM) paired with CL spectroscopy. Finally, the size-dependent thermal instability induced formation mechanism was proposed.

Experimental Methods

Synthesis Methods

The ZNW templates were grown on a ZnO-film-coated silicon substrate using a vapor phase transport, as we previously reported [12]. The synthesis of ZSO nanotube arrays was carried out in a vacuum tube furnace with an outer diameter of 24 mm and a length of 1,200 mm. A 0.2 g powder mixture of SiO_2 (Alfa Aldrich, 99.9%), activated carbon (as a reductant), and Si with equal molar ratios was placed at the center of the tube. A piece of the ZNW template was placed downstream of the tube at $\sim$14 cm away from the source. The tube was sealed and evacuated to a base pressure of $\sim$2 Pa. The furnace was then heated to 1,100°C at a rate of 24°C min^{-1} and kept at this temperature for 2 h. The local temperature of the substrate was about 1,000°C due to the temperature gradient along the tube furnace. A constant flow of high-purity Ar gas was fed into the tube at a flow rate of 80 sccm (standard cubic centimeters per minute) and a pressure of 100 Torr throughout entire heating/cooling. After the furnace was naturally cooled to room temperature, the surface color of ZNW templates changed from black to white–gray.

Characterization Tools

The ZNW templates and ZSO samples were characterized by a powder X-ray diffraction (XRD; Rigaku, Ultima III, 40 kV/40 mA with Cu K_α radiation), a scanning electron microscope (SEM; JEOL, JSM-6700F), a high-resolution field-emission transmission electron microscope (TEM; JEOL, JEM-3000F), a high-angle annular dark-field scanning transmission electron microscope detector (HAADF-STEM) (JEOL JEM-3100FEF), and an energy-dispersive X-ray spectrometer (EDX). CL spectra were recorded at room temperature in an ultrahigh-vacuum SEM with a Gemini electron gun (Omicron, Germany) at an accelerating voltage of 10 kV and a current of 1 nA.

Results and Discussion

Vertically aligned ZNW arrays with an underlayer of interconnected nanowalls were grown on a ZnO buffer layer [12]. The ZNWs have typical diameters of $\sim$30–150 nm and lengths of $\sim$10 μm. Cross-sectional view SEM images (Fig. 1a, c) revealed that the ZSO arrays keep the vertical alignment peculiar to the ZNW templates and protrude from the underlayer nanowall networks. The top-view SEM images (Fig. 1b, d) clearly indicate that the nanotube diameters are larger than those of ZNW due to SiO_x coatings. The originally separated ZNWs stick to each other after thermal annealing. Hollow tube morphologies can be clearly seen from the top-view SEM image of the ZSO sample after scratching off the surface nanotubes (inset of Fig. 1d). The XRD spectrum of the ZNW arrays displays only one strong (002) peak due to their high c-axis orientation growth. A strong diffraction peak at 34.02° and other four relatively weak peaks in the XRD spectrum (Fig. 2) of the ZSO sample can be indexed to a rhombohedral Zn_2SiO_4 crystal structure with the lattice constants of $a = b = 1.394$ nm and $c = 0.9309$ nm (JCPDS Card: 08-0492). The ZnO (002) peak coming from the ZnO buffer layer can also be seen.

Detailed crystal structure and compositional analyses of the ZSO samples were carried out by TEM and EDS. Three types of tube morphologies, i.e., discrete particles encapsulated tubes, hollow tubes, and tubes only partially filled with nanoparticles, were observed (Fig. 3a). All the nanotubes including their tip-ends have a uniform SiO_x ($x < 2$, as measured by EDS, see supporting Figure S1) shell layer (the inset TEM image of Fig. 3b). High-magnification and high-resolution TEM observations (HRTEM) and selected area electron diffraction (SAED) patterns reveal that the as-synthesized ZSO samples consist of three types of tubular morphologies depending on their diameters (Fig. 3b), as shown in Fig. 3c, f, and i, respectively. The nanotubes ($\sim$20%) with diameters $\sim$50–100 nm have usually an amorphous SiO_x ($\sim$20 nm) outer shell and an inner tube (diameter $\sim$30 nm) made of polycrystalline Zn_2SiO_4 particles (Fig. 3c). The polycrystalline nature of the inner tube was confirmed by HRTEM imaging and SAED patterns (Fig. 3d, e). The weak lattice fringes in Fig. 3e with a d-spacing of 1.62, 2.53, 2.63, and 2.83 Å can also be observed. These correspond to a rhombohedral Zn_2SiO_4 phase (r-Zn_2SiO_4) and (315), (042), (410), and (113) planes

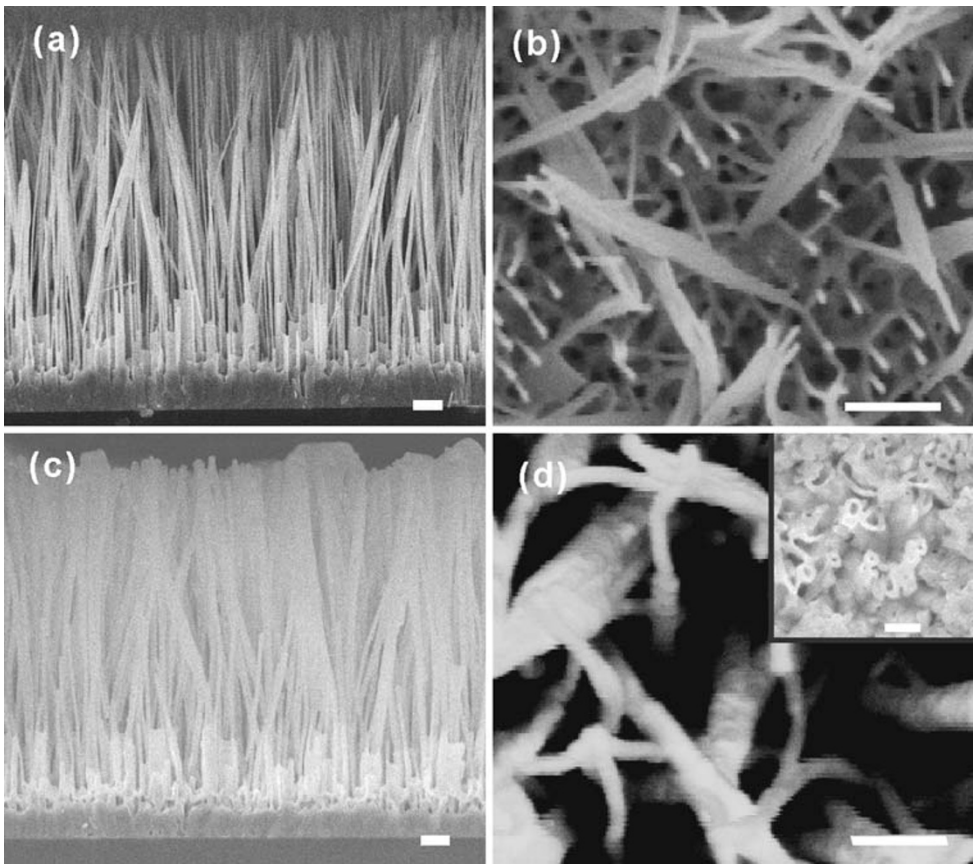

Fig. 1 SEM images of **a**, **b** a ZNW template and **c**, **d** a ZSO sample. The *inset* top-view SEM image shows the ZSO sample after scratching surface nanotubes out of the substrate. The *scale bars* in **a**–**d** are 1 μm and for the *inset* is 500 nm. **a**, **c** cross-sectional view images, **b**, **d** top-view images

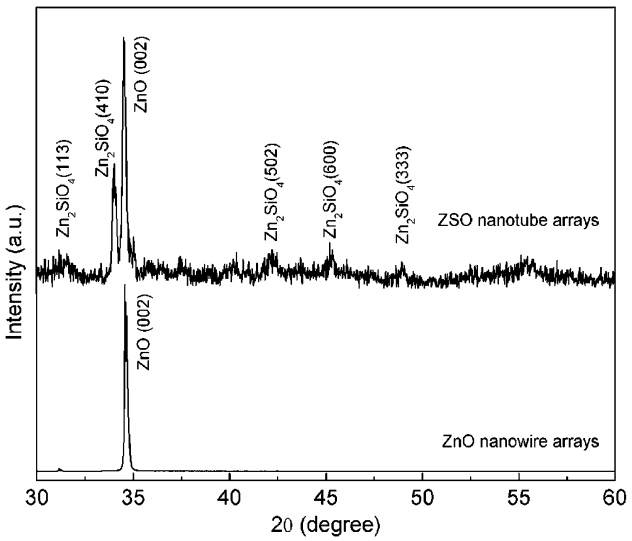

Fig. 2 Comparative XRD spectra of a ZNW template and a ZSO sample

of it. About 40% of nanotubes with diameters of ~90–160 nm have a unique morphology of single-crystalline Zn_2SiO_4-nanoparticle chains encapsulated into a SiO_x nanotube. The SAED pattern in Fig. 3h recorded from an embedded rod-shaped nanoparticle can be indexed to the $[\bar{2}\bar{2}1]$ zone of *r*-Zn_2SiO_4 and confirms the single-crystalline character of the particle. The nanoparticles are partially surrounded by a thin amorphous SiO_x layer (~5 nm thick), as seen in Fig. 3g. The other ~40% nanotubes with outer diameters larger than ~150 nm were found to be SiO_x-coated single-crystalline Zn_2SiO_4 nanotubes. The corresponding HRTEM image and SAED pattern (Fig. 3j, k) verify that an *r*-Zn_2SiO_4 nanotube is a single crystal. The adjacent lattice fringes separated by 2.83, 4.02, and 7.02 Å and labeled in Fig. 3d, g, and j correspond to the interplanar distances of (113), (300), and (110) planes in Zn_2SiO_4, respectively. This fact is consistent with the XRD results shown in Fig. 2.

The spatial distribution of Zn, Si, and O species was mapped using corresponding EDX K_α emissions in the HAADF-STEM mode. Due to a large difference in atomic numbers between Zn and Si, a HAADF-STEM image in Fig. 4a clearly reveals the typical structural features of a Zn_2SiO_4-nanoparticle-encapsulated SiO_x nanotube, and a SiO_x-coated Zn_2SiO_4 coaxial nanotube. As shown in the spatially resolved elemental maps in Fig. 4, Zn species are only present within encapsulated nanoparticles and the inner shell of the Zn_2SiO_4-SiO_x coaxial nanotube.

CL spectroscopy combined with SEM imaging has been proven to be a powerful tool for probing the local characteristics of low-dimensional materials due to its high

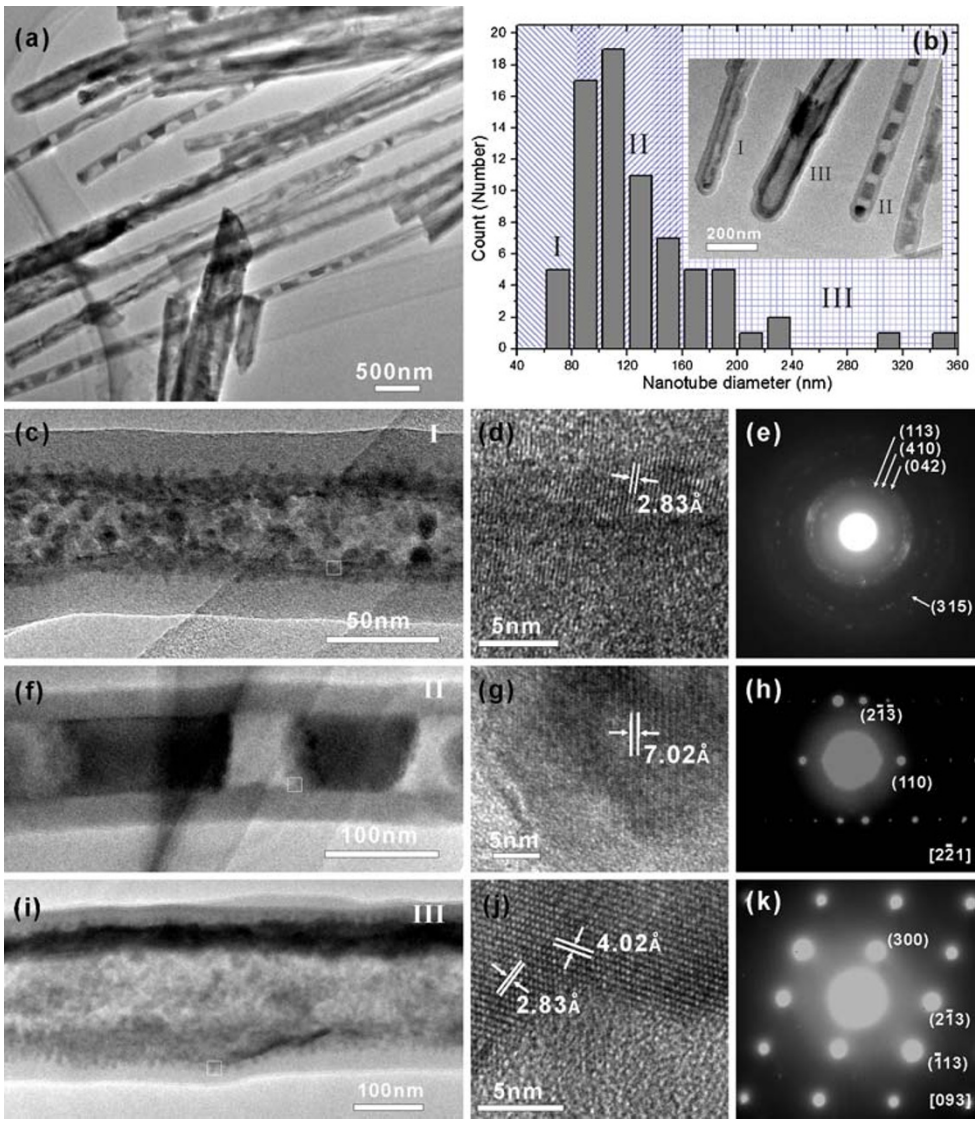

Fig. 3 **a** Low-magnification TEM image of nanotubes; **b** Histogram of the diameter distribution based on 70 randomly selected nanotubes. The *inset* shows tip-end TEM images for the three types of nanotubes. **c** High-magnification TEM images, type I: a SiO_x-coated polycrystalline Zn_2SiO_4 nanotube, **f** type II: a SiO_x nanotube periodically encapsulated with single-crystalline Zn_2SiO_4 nanoparticles, and **i** type III: a SiO_x-coated single-crystalline Zn_2SiO_4 nanotube; **d**, **g**, and **j** corresponding HRTEM images taken from the *framed areas* marked in (**c**), (**f**), and (**i**), respectively; (**e**) and (**k**) corresponding SAED patterns taken from the nanotubes shown in (**c**) and (**i**), respectively. (**h**) SAED pattern taken from the encapsulated nanoparticle in (**f**). The diameter distributions for type I, II, III nanotubes are labeled in different sectors in (**b**)

spatial resolution (a submicrometer range) [13, 14]. This makes CL a valuable nondestructive tool for studies of inhomogeneities in nanostructures caused by doping or growth condition variations. We attempted to use CL spectroscopy to detect and analyze the Zn_2SiO_4 phase in the ZSO samples. The CL spectrum recorded from the ZSO sample cross-section is shown in the inset of Fig. 5b. The emission peak at 310 nm (4.0 eV) with a shoulder at 280 nm (4.4 eV, see fitting curve of supporting Figure S2), which is well below the band gap 5.4 eV of Zn_2SiO_4, is attributed to the radiation recombination from the Zn_2SiO_4 phase, considering that the similar emission peak at 300 nm (4.13 eV) was previously reported for the Zn-Zn_2SiO_4 nanocables [15]. The 380 nm emission peak can be ascribed to the near-band-edge recombination of a crystalline ZnO buffer layer. These two sharp emission peaks may result from the single-crystalline characters of Zn_2SiO_4 and ZnO phases, respectively. From the CL spectra recorded in different spots, indicated in Fig. 5b, the intensity of peaks at 380 nm shows a dramatic decrease from the ZnO buffer layer toward the nanotubes; the opposite trend is in effect for the emission at 310 nm. This indicates that all crystalline ZNWs have been totally consumed during annealing. The 380 nm emission only comes from the ZnO buffer layer. The weak violet emission at 440 nm can be rationally assigned to a SiO_x phase [16], and the broad emission band at 550 nm can be ascribed to the Zn_2SiO_4 phase. Note that there is also report on the assignment of 440 and 550 nm emission bands to the related defect emission of ZnO [17]. The corresponding CL emission images recorded for each peak are shown in Fig. 5c–f. The 310 nm CL emission image (Fig. 5c), combined with the 550 nm emission image in Fig. 5f, shows the inhomogeneous distribution of the Zn_2SiO_4 phase, i.e., stronger intensities for the underlayer nanowalls (which have a larger size compared to the top nanotube

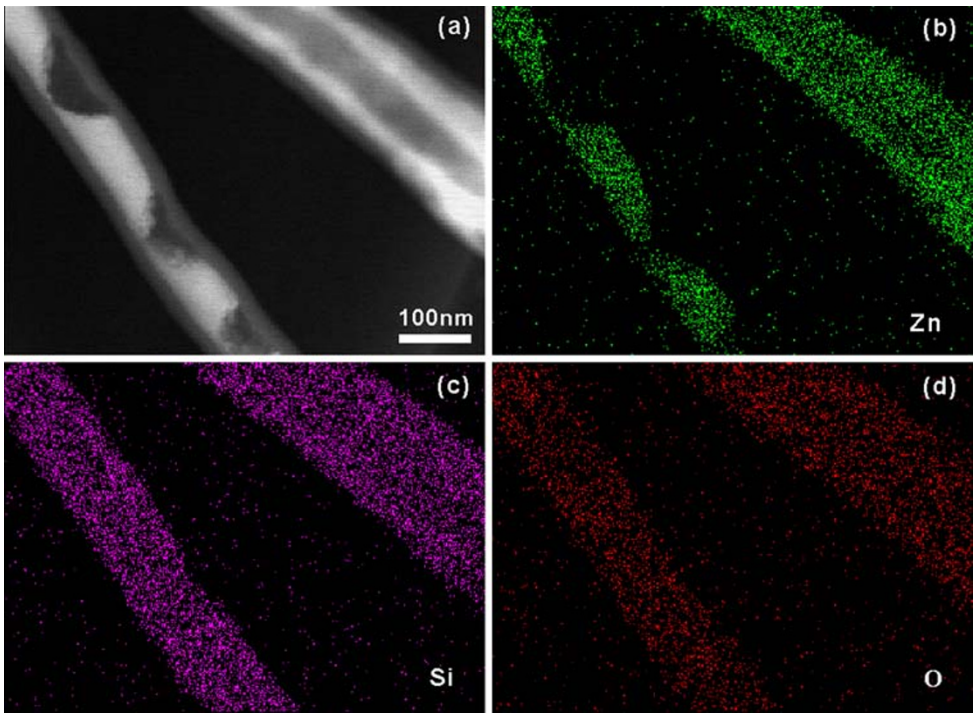

Fig. 4 **a** HAADF-STEM image of two typical Zn_2SiO_4 nanotube morphologies, a SiO_x-shelled Zn_2SiO_4 nanochain-encapsulated nanotube (*left*) and a SiO_x-coated Zn_2SiO_4 nanotube (*right*); **b**, **c**, and **d** the corresponding spatially resolved elemental EDS maps of Zn, Si, and O

portions). The uniform 440 nm emission image is consistent with the TEM observation of a homogeneous SiO_x coating. The assignment of 310 and 550 nm emissions was further confirmed by the emission from the interface between a ZnO buffer layer and a Si substrate, as indicated by arrows in Fig. 5c, f. One can expect that the reaction between the ZnO film and the surface SiO_x layer on a Si substrate can lead to Zn_2SiO_4 phase formation during high-temperature annealing [18].

The further high-magnification CL images were recorded from representative nanotubes dispersed on a TEM grid. Owing to the high sensitivity and high spatial resolution of the CL spectroscopy mapping, the nanotubes with almost same elemental compositions but different morphologies can readily be indentified at a large scale. As shown in Fig. 6c, strong 310 nm CL emission comes from both the embedded Zn_2SiO_4 nanopaticles (type II) and Zn_2SiO_4 nanotubes of larger size (type III), while smaller SiO_x-coated Zn_2SiO_4 nanotubes (type I) only show hardly detectable emission. These results are in a good agreement with TEM characterization. Also, they further confirm the above-mentioned peak assignment.

It will be of interest to investigate the formation mechanism during simultaneous generation of different tube structures, especially regarding the Zn_2SiO_4-nanoparticle chains, for the first time observed here in a ternary compound nanomaterial. We believe that nanoscale thermodynamics of ZNW is an important factor. It has been experimentally demonstrated that the melting point of Cu, Zn, and Sn nanowires will significantly decrease with a decrease in wire diameter [19–21]. Based on molecular dynamics simulations, the same diameter dependency has also been found for GaN nanowires [22]. In addition, under heating in air, ZnO nanorods start to melt at 750°C, [23] much lower temperature than the melting point of a bulk form. Therefore, it is reasonable to assume that the melting point of ZNW would also decrease with diameter decreasing.

Based on the above-mentioned assumption and taking the results of XRD, TEM, EDS, and CL measurements, we conclude that the factors responsible for the different tube morphologies are the size-dependent melting behavior of ZnO and the competition between surface and volume diffusions. Since the Si atom has nearly the same radius as the Zn atom and the bonding energy of the Si–O bond (185 kJ/mol) is about two times higher than that of the Zn–O bond (92 kJ/mol), it is easy for ZnO to diffuse into SiO and to form a Zn_2SiO_4 phase, as reported by Wang and Zhou [11, 25]. It is also noted that the ZNW template was totally decomposed in a control experiment under the same heating process but without introducing a source powder. The formation mechanism here is illustrated in Fig. 7, and the three predominated effects decomposition of "etching", the Rayleigh instability, and the Kirkendall solid-state reaction are highlighted for the nanotubes of type I, II, and III, respectively. During the temperature increase, the Si–O vapor (sublimated from the source) can quickly be transported and deposited on the nanowire surfaces, preventing their decomposition. Rapid heating quickly drives the system to high temperature. The ZNWs with smaller

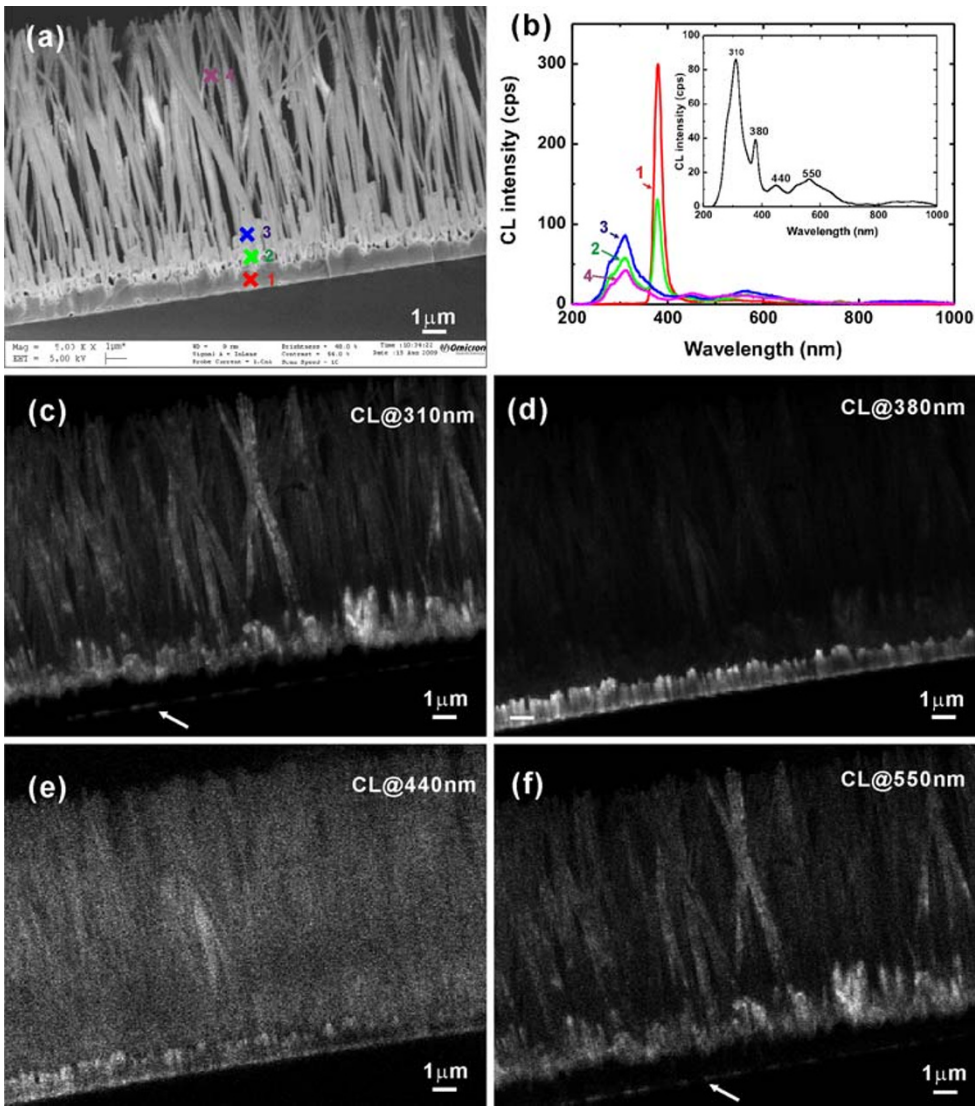

Fig. 5 **a** Cross-sectional view SEM image of a ZSO sample and corresponding room-temperature CL spectrum in (**b**); **c**, **d**, **e**, and **f** CL images of the array under the 310, 380, 440, and 550 nm emissions, respectively

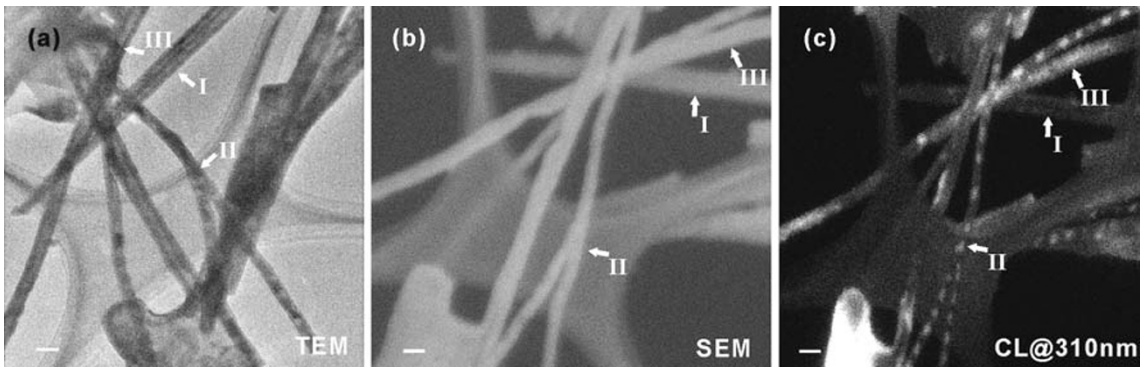

Fig. 6 **a**, **b**, and **c** TEM and SEM images, and corresponding 310 nm CL emission image of representative nanotubes dispersed on a TEM grid. Three nanotube types are labeled as I, II, and III, and indicated by *arrows*, respectively. Note that type I nanotubes consist of two nanotubes of small diameter. The *scale bars* are 200 nm

diameters (<60 nm, estimated from the above TEM statistical analysis), which possess lower melting temperatures, prefer to decompose into Zn vapor and O_2 rather than to react with Si forming Zn_2SiO_4. The ZnO deficiency and SiO_x richness at the interface lead to the formation of a thin polycrystalline Zn_2SiO_4 layer on the inner surface of the

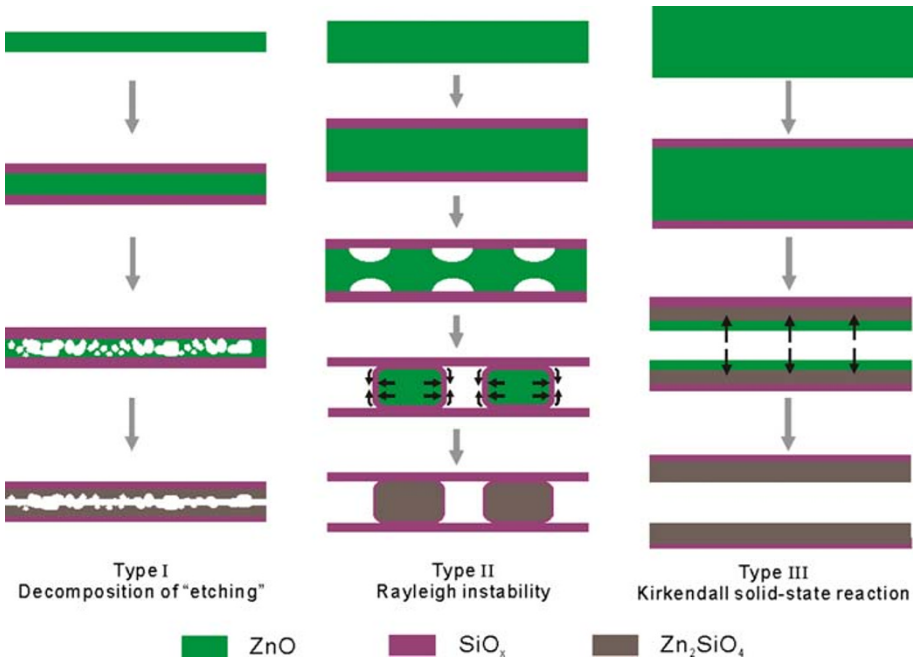

Fig. 7 Schematics of the formation mechanism for three discovered types of tubular structures

SiO_x shell. The ZNWs with medium diameters (~60–120 nm) prefer melting rather than decomposition. In accord with the Rayleigh instability effect, [19, 24] the ZnO liquid cylinder of radius r is unstable to radius perturbations whose wavelength l exceeds the circumference of the cylinder. The cylinder thus decreases its total energy and breaks into nanoparticles under surface tension. As the ZnO liquid starts to shrink, the Si/O surface diffusion will rapidly increase around the curved portions, since the surface diffusion of atoms is proportional to the gradient of the wire surface curvature at a certain temperature [26]. Subsequent volume diffusion at the interface and subsequent reactions lead to single-crystalline Zn_2SiO_4-nanoparticle chains encapsulated into SiO_x nanotubes. The ZNWs with larger diameters (>120 nm) will be in a thermally unstable solid state. Unequal diffusion rates for the outward Zn/O and inward Si/O, known as the Kirkendall diffusion, [4–6] produce a hollow interior along the structure length. The SiO_x coating is thicker than necessary for complete consuming of the interior ZnO to form a new phase. As a result, SiO_x-coated single-crystalline Zn_2SiO_4 coaxial nanotubes are formed. Note that due to the diameter nonuniformity of an individual wire, nanotubes with partial nanoparticle encapsulation may also form, as shown in Fig. 3a.

It is worth mentioning that by using plasma-enhanced chemical vapor deposition (PECVD) of a thin amorphous Si film (~10 nm) on the top half of a ZNW template followed by vacuum annealing, Zhou et al. [11] fabricated vertically aligned Zn_2SiO_4 nanotube/ZnO nanowire heterojunction arrays. Our results undoubtedly demonstrate that prior to ZnO template utilization for reliable making ternary compound nanotubes, problems associated with their thermal instability must be seriously taken into account and solved. The good news is that due to many diameter-controllable synthesis methods of ZNWs reported to date, finding templates with uniform diameters for the subsequent unique one specific ternary nanotube syntheses looks highly plausible. Furthermore, the Rayleigh instability applied to ZNW provides a structuring technique that produces long chains of ZnO-based compound semiconducting nanospheres which may find potential applications in nanoscale photonic devices [27].

In conclusions, vertically aligned Zn_2SiO_4-nanoparticle chains encapsulated into SiO_x nanotubes, SiO_x-coated polycrystalline and single-crystalline Zn_2SiO_4 coaxial nanotubes were simultaneously fabricated by a one-step solid-state reaction using ZNW array templates. It is found that the nanotubes of different morphologies can be easily identified by CL spectroscopy mapping technique. The apparent size-dependent nonuniform nanotube generation was due to the strong size-dependent thermodynamic behavior of ZNWs. With diameter increasing of starting ZNW, the formation mechanism changes from decomposition of "etching", to Rayleigh instability, and then to Kirkendall effect, resulting in polycrystalline Zn_2SiO_4-SiO_x coaxial nanotubes, single-crystalline Zn_2SiO_4-nanoparticle-chain-embedded SiO_x nanotubes, and single-crystalline Zn_2SiO_4-SiO_x coaxial nanotubes, respectively.

Acknowledgments This work was supported by the World Premier International Center for Materials Nanoarchitectonics (MANA) Project tenable at the National Institute for Materials Science (NIMS), Tsukuba, Japan. The authors thank Drs. A. Nukui, M. Mitome, and Mr. K. Kurashima for the continuous technical support and kind help.

References

1. M.S. Dresselhaus, Y.M. Lin, O. Rabin, A. Jorio, A.G.S. Filho, M.A. Pimenta, R. Saito, G.G. Samsonidze, G. Dresselhuas, Mater. Sci. Eng. C **23**, 129 (2003)
2. Y. Xiong, B. T. Mayers, Y. Xia, Chem. Commun. 5013 (2005)
3. H.C. Zeng, J. Mater. Chem. **16**, 649 (2006)
4. H.J. Fan, U. Gösele, M. Zacharias, Small **3**, 1660 (2007)
5. H.J. Fan, Y. Yang, M. Zacharias, J. Mater. Chem. **19**, 885 (2009)
6. C. Yan, D. Xue, Adv. Mater **20**, 1055 (2008)
7. J. Goldberger, R.R. He, Y.F. Zhang, S.W. Lee, H.Q. Yan, H.J. Choi, P.D. Yang, Nature **422**, 599 (2003)
8. J. Zhou, J. Liu, J. Yang, R.S. Lao, C.S. Gao, R. Tummala, N.S. Xu, Z.L. Wang, Small **2**, 1344 (2006)
9. C. Yan, D. Xue, J. Phys. Chem. B **110**, 25850 (2006)
10. K. Wang, J. Chen, W. Zhou, Y. Zhang, Y. Yan, J. Pern, A. Mascarenhas, Adv. Mater **20**, 3248 (2008)
11. J. Zhou, J. Liu, X.D. Wang, J.H. Song, R. Tummala, N.S. Xu, Z.L. Wang, Small **4**, 622 (2007)
12. C. Li, G.J. Fang, J. Li, L. Ai, B.Z. Dong, X.Z. Zhao, J. Phys. Chem. C **112**, 990 (2008)
13. S.I. Maximenko, L. Mazeina, Y.N. Picard, J.A. Freitas Jr., V.M. Bermudez, S.M. Prokes, Nano Lett. **9**, 3245 (2009)
14. X.L. Yuan, B. Dierre, J.B. Wang, B.P. Zhang, T. Sekiguchi, J. Nanosci. Nanotech. **7**, 3323 (2007)
15. X. Feng, X. Yuan, T. Sekiguchi, W. Lin, J.Y. Kang, J. Phys. Chem. B. **109**, 15786 (2005)
16. D.P. Yu, Q.L. Hang, Y. Ding, H.Z. Zhang, Z.G. Bai, J.J. Wang, Y.H. Zou, W. Qian, G.C. Xiong, S.Q. Feng, Appl. Phys. Lett. **73**, 3076 (1998)
17. A.B. Djurisic, Y.H. Leung, Small **2**, 944 (2006)
18. X. L. Xu, P. Wang, Z. M. Qi, H. Ming, J. Xu, H. T. Liu, C. S. Shi, G. Lu, W. K. Ge, J. Phys.: Condens. Matter. **15**, L607 (2003)
19. M.E.T. Molares, A.G. Balogh, T.W. Cornelius, R. Neumann, C. Trautmann, Appl. Phys. Lett. **85**, 5337 (2004)
20. X.W. Wang, G.T. Fei, K. Zheng, Z. Jin, L.D. Zhang, Appl. Phys. Lett. **88**, 173114 (2006)
21. H.S. Shin, J. Yu, J.Y. Song, Appl. Phys. Lett. **91**, 173106 (2007)
22. W. H. Moon, H. J. Kim, C. H. Choi, Scr. Mater. **56**, 345 (2007)
23. X. Su, Z. Zhang, M. Zhu, Appl. Phys. Lett. **88**, 061913 (2006)
24. Y. Qin, S.M. Lee, A. Pan, U. Gösele, M. Knez, Nano Lett. **8**, 114 (2008)
25. H.Q. Wang, G.Z. Wang, L.C. Jia, C.J. Tang, G.H. Li, J. Phys. Chem. C. **111**, 14307 (2007)
26. F.A. Nichols, W.W. Mullins, Trans. Metall. Soc. AIME **233**, 1840 (1965)
27. Y. Zhu, H.I. Elim, Y.-L. Foo, T. Yu, Y. Liu, W. Ji, J.-Y. Lee, Z.A. Shen, T.S. Wee, J.T.L. Thong, C.H. Sow, Adv. Mater. **5**, 587 (2006)